DOI: 10.1002/((please add manuscript number))
Article type: Full Paper

Anomalous low thermal conductivity of atomically thin InSe probed by scanning thermal microscopy

David Buckley, Zakhar R. Kudrynskyi, Nilanthy Balakrishnan, Tom Vincent, Debarati Mazumder, Eli Castanon, Zakhar D. Kovalyuk, Oleg Kolosov, Olga Kazakova, Alexander Tzalenchuk, and Amalia Patanè**

Dr. D. Buckley, T. Vincent, E. Castanon, Dr. O. Kazakova, Prof. A. Tzalenchuk
National Physical Laboratory, Hampton Road, TW11 0LW, Teddington, United Kingdom

Dr. Z. R. Kudrynskyi, D. Mazumder, Prof. A. Patanè
School of Physics and Astronomy, University of Nottingham, NG7 2RD, Nottingham, United Kingdom
E-mail: zakhar.kudrynskyi@nottingham.ac.uk
E-mail: amalia.patane@nottingham.ac.uk

Dr. N. Balakrishnan
National Graphene Institute, The University of Manchester, M13 9PL, Manchester, United Kingdom
School of Chemical and Physical Sciences, Keele University, ST5 5BG, Keele, United Kingdom

Prof. Z. D. Kovalyuk
Institute for Problems of Materials Science, The National Academy of Sciences of Ukraine, Chernivtsi Branch, 58001, Chernivtsi, Ukraine

Prof. O. Kolosov
Department of Physics, Lancaster University, LA1 4YB, Lancaster, United Kingdom

Keywords: InSe, 2D semiconductors, scanning thermal microscopy, thermal conductivity, phonons

The ability of a material to conduct heat influences many physical phenomena, ranging from thermal management in nanoscale devices to thermoelectrics. Van der Waals two dimensional (2D) materials offer a versatile platform to tailor heat transfer due to their high surface-to-volume ratio and mechanical flexibility. Here, the nanoscale thermal properties of 2D indium selenide (InSe) are studied by scanning thermal microscopy. The high electrical conductivity, broad-band optical absorption and mechanical flexibility of 2D InSe are accompanied by an anomalous low thermal conductivity (κ). This can be smaller than that of low-κ dielectrics, such as silicon oxide, and it decreases with reducing the lateral size and/or thickness of InSe. The thermal response is probed in free-standing InSe layers as well as layers supported by a substrate, revealing the role of interfacial thermal resistance, phonon scattering, and strain. These thermal properties are critical for future emerging technologies, such as field effect transistors that require efficient heat dissipation or thermoelectric energy conversion with low-κ, high electron mobility 2D materials, such as InSe.

1. Introduction

Atomically thin layers of van der Waals (vdW) crystals and their heterostructures offer a versatile two-dimensional (2D) materials base for quantum science and innovative technologies.[1-4] The compatibility of 2D vdW crystals and heterostructures with a wide range of metals and dielectric substrates can overcome limitations of traditional semiconductor heterojunctions (*i.e.* material and substrate incompatibility due to lattice mismatch, defected interfaces, *etc.*) enabling innovative ways to manipulate charge, spin and phonon quanta at the nanoscale, with prospects for miniaturized, high-performance functional devices. Amongst the 2D materials in the metal chalcogenide class, indium selenide (InSe) has emerged as a promising semiconductor.[5-14] It has a band edge absorption energy that increases with decreasing layer thickness;[5-6] high broad-photoresponsivity from the infrared (IR) to the ultra-violet (UV) range;[7-9] low-mass conduction band electrons and high electron mobility even in atomically thin films (*i.e.* larger than in silicon-based field effect transistors (FETs));[10-11] high mechanical strength;[12-13] a strain-sensitive band structure[14-15] with 1D van Hove singularities[16], *etc*. Thanks to this unique set of physical properties, 2D InSe holds promise for a wide range of applications, from ultra-thin and flexible electronics to next-generation quantum metrology and photosensing.[15, 17-23]

The science and technology of 2D InSe is a rapidly developing field. However, the investigation of phonon transport and thermal properties of 2D InSe is still in its infancy.[24-33] Although theoretical studies have provided an insight into the thermal conductivity (κ) of 2D InSe, the experimental investigation of heat transport at the nanoscale is rarer, as it requires advanced microscopy imaging techniques. Furthermore, real device structures involve heat transfer across interfaces and lateral boundaries that are generally ignored by theory. Phonon transport underpins a plethora of physical phenomena, ranging from heat conduction and thermal insulation to energy conversion. Thus, they play a key role in several emerging

applications. For example, a low thermal conductivity represents a drawback to heat dissipation in miniaturized FETs, but is desirable for thermoelectric energy conversion.

Here, we use scanning thermal microscopy (SThM)[34-35] to probe and image the thermal response of 2D InSe with nanoscale resolution. We present studies on atomically thin InSe flakes with different thickness and/or in-plane area. The SThM study reveals a low-κ for both free-standing InSe layers and layers supported by different substrate materials, such as low-κ silicon dioxide (SiO_2) and polymethyl methacrylate (PMMA), as well as high-κ hexagonal boron nitride (hBN). The thermal response is influenced by phonon scattering at edges and interfaces of 2D InSe, as well as strain and thermal coupling of InSe to its supporting substrate. We show that these phenomena become prominent in atomically thin layers and weakly thermally coupled interfaces.

2. Results and Discussion

2.1. Scanning Thermal Microscopy of 2D InSe

Figure 1a illustrates a schematic of the experimental setup used for the ambient SThM studies of γ-InSe flakes containing a different number of layers (L) and with different in-plane area (A). The SThM is a specific scanning probe microscopy mode, which uses a thermal probe. The probe is a part of a biased Wheatstone bridge,[34, 36] which comprises two known resistors (R_1 and R_2), a variable resistor (R_3) and the thermal probe resistor (R_{probe}) of the SThM tip (see Experimental Section for details). The apex of the SThM probe acts as a local heater of the InSe flake. When the probe is brought into close contact with the flake surface, the probe's temperature decreases due to the heat transfer to the sample, leading to a reduced resistance R_{probe} that unbalances the bridge, as monitored by the output voltage V_{out}:

$$V_{out} = gV_S\,[R_{probe}/(R_{probe}+R_1)-R_3/(R_2+R_3)], \quad (1)$$

where g is the gain of the non-inverting amplifier and V_s is the voltage applied to the bridge (see Figure 1a). When the probe resistance R_{probe} decreases due to cooling of the tip, the output voltage V_{out} changes. The corresponding change of electrical power dissipated by the probe resistor, $\Delta P = R_{probe}\,\Delta V_{out}$, is proportional to the heat flux towards the sample and its thermal conductivity, but it is also influenced by the heat loss from the cantilever, air conduction/convection, tip-sample interfacial thermal resistance and heat propagation radius (see Experimental Section). In contrast to far-field optical techniques, such as Raman spectroscopy, SThM is not limited by optical diffraction and can image the thermal response of a sample with high spatial resolution (down to 50 nm). This is essential for thermal studies of 2D InSe flakes with different size and/or edges, and systems where the layers are supported by a substrate with a spatially varying topography, as described in the following sections.

2.2. InSe on a SiO_2/Si substrate

γ-InSe flakes of different thickness, down to a single layer, *i.e.* $L = 1$ (nominally thickness of 0.83 nm), were mechanically exfoliated on a SiO_2/Si (290 nm-thick SiO_2) substrate (see inset of Figure 1a and Experimental Section). Figure 1b displays the atomic force microscopy (AFM) and SThM images for a representative InSe flake. The flake consists of two regions with $L = 1$ (measured thickness $t = 0.9\pm0.5$ nm) and $L = 5$ ($t = 4.0\pm0.6$ nm). In the SThM image, the InSe layers appear in red-orange on the dark-blue background of the SiO_2 substrate, indicating that InSe has a lower thermal conductivity than SiO_2. The measured voltage, V_{out}, is scaled relative to that of SiO_2, V_{SiO2}, which is constant in different experiments and so set as a reference value, *e.g.* $V_{SiO2} = 0$ V. The associated standard deviation, ΔV_{SiO2}, of the mean value of V_{SiO2} is then used to assess the experimental uncertainty of the SThM response. To show this in more detail, Figure 1c illustrates a profile of $V_{out} - V_{SiO2}$ along the line marked on the SThM image of Figure 1b. Here, positive values of

V_{out} -V_{SiO2} correspond to regions of InSe on the SiO_2 substrate. Also, larger values of V_{out} -V_{SiO2} correspond to smaller κ.

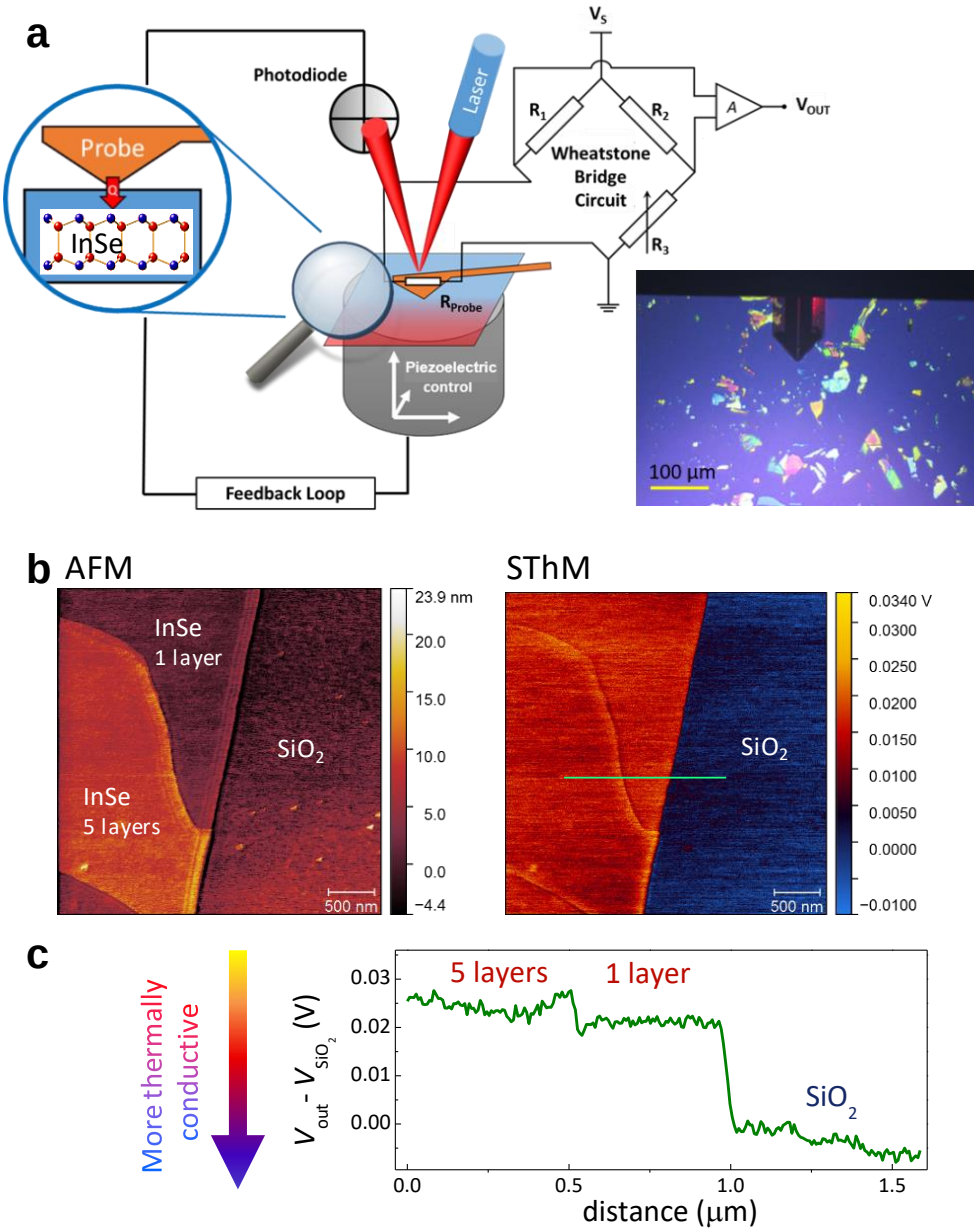

Figure 1. Scanning Thermal Microscopy (SThM) of 2D InSe. **(a)** SThM set-up showing the SThM probe as a resistor in a Wheatstone bridge. The SThM tip heats up due to the flowing current and transfers heat onto the sample. As a result, the tip cools down and changes its resistance, which is monitored by the output voltage V_{out}. Inset: optical image of InSe flakes on a SiO_2/Si substrate. The SThM tip is visible on the top of the image. **(b)** Left: AFM image showing an exfoliated InSe flake on a SiO_2/Si substrate. The flake consists of single and 5 layers InSe. Right: SThM image acquired simultaneously to the AFM image. Here, larger output voltages correspond to lower thermal conductance values. The line marks the SThM profile shown in part **(c)**.

The SThM image indicates that the ability of the InSe flake to dissipate heat from the SThM tip is lower than that of SiO_2, which is known to have a low κ (κ_{SiO2} ~1.4 W m^{-1} K^{-1} at T = 300 K).[37] Our observations contrast with previous experiments on bulk crystals of InSe, which reported values of in-plane κ from 10.42 W m^{-1} K^{-1} to 12 W m^{-1} K^{-1} at T = 300 K. [38-40] To interpret these results, we note that the ability of a material to conduct heat is influenced by many factors, including its thickness, lateral size, state of the surface,[36, 41] and, notably, the direction of heat propagation that can be a dominating factor in anisotropic materials, such as γ-InSe. For example, for bulk γ-InSe, the room temperature in-plane κ(10.42 W m^{-1} K^{-1}) is 6 times larger than the out-of-plane κ (1.74 W m^{-1} K^{-1}) due to the weak vdW bonding between the layers typical of 2D materials.[38, 42] Also, the measured SThM signal can be affected by the thermal resistance of the flake interface with other materials and/or supporting substrate, the thermal conductivity of the substrate and the tip-surface thermal resistance.[43-45] We examine these phenomena by thermal microscopy studies of different InSe-based structures.

Figures 2a and b show the AFM and SThM images of a large area sample containing over 100 InSe flakes with different number of layers (L > 15) and in-plane area (A < 10 μm^2). Individual flakes were identified from the AFM images using an Otsu thresholding[46] and corresponding masks were then applied to the SThM maps to correlate specific features in the SThM and AFM images. From this systematic analysis, we extract the data in Figure 2c, showing the SThM response as a function of A for samples with L >15 layers. We note that for this analysis we used data from the central area of the flake to avoid artefacts arising from the signal variation at the edge of the flake due to the a reduced contact area as well as directionality of heat propagation in the anisotropic flake.[47] These data indicate that the SThM response depends strongly on the flake area, with large values of V_{out} -V_{SiO2} (hence, smaller thermal conductance) for small area layers with A < 2 μm^2.

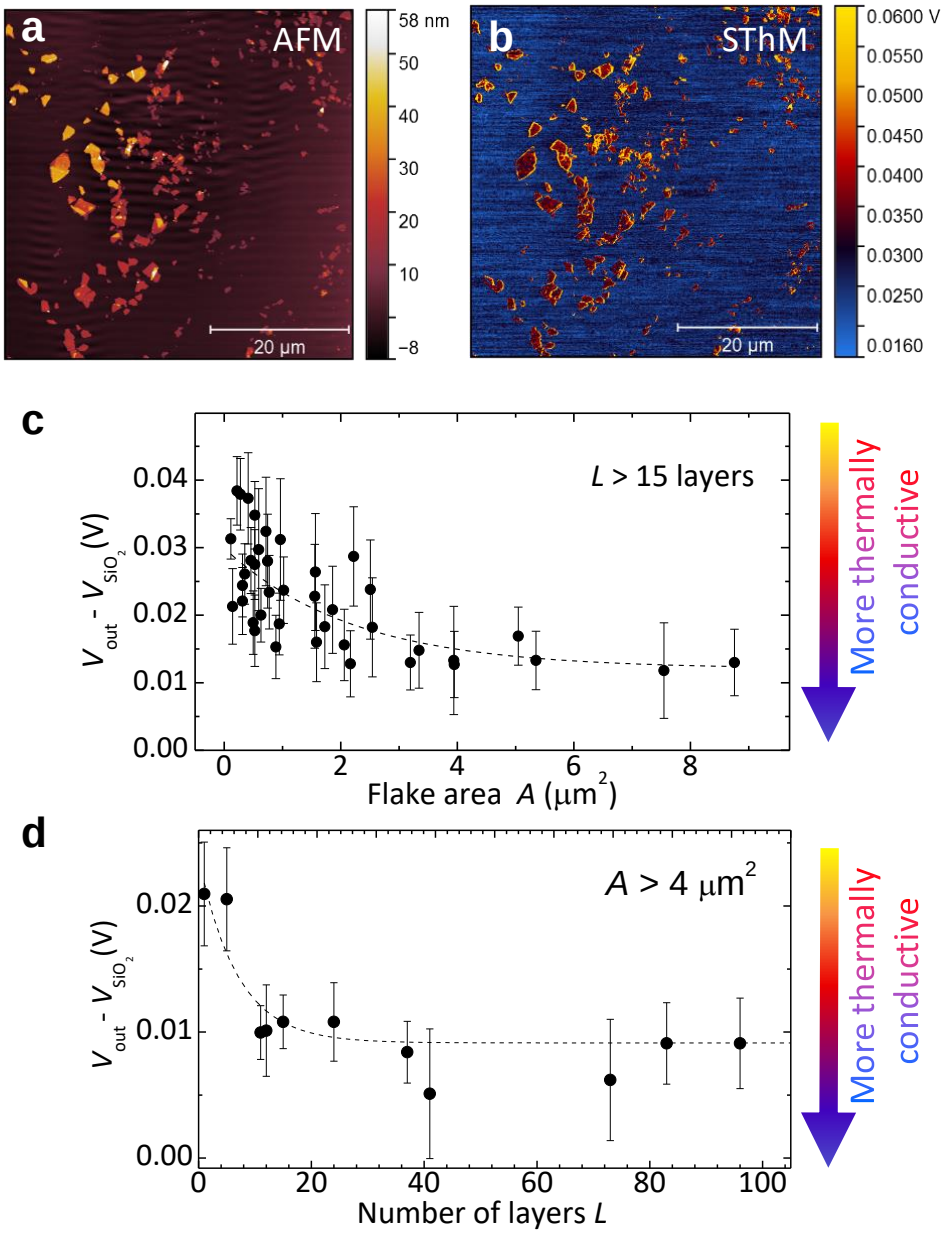

Figure 2. Thermal properties of InSe flakes on a SiO_2/Si substrate. AFM **(a)** and SThM **(b)** images of InSe flakes with different areas (A) and number of layers (L) on a SiO_2/Si substrate. **(c-d)** SThM response as a function of A (L > 15 layers) **(c)** and L (A > 4 μm^2) **(d)**. Dashed lines are guides to the eye.

To explore the thickness dependence of the SThM response, in Figure 2d we examine InSe flakes with A > 4 μm^2 and L ranging from 1 to 100 layers. The choice of relatively large area flakes avoids conflating a dependence on thickness with a dependence on area. This study shows that the value of V_{out} -V_{SiO2} is similar for flakes thicker than 10 layers, but doubles

in a few layer (L = 1- 5) flakes, indicating a reduced thermal conductance in atomically thin layers. In these experiments, while we can safely assume that the tip-sample and sample-substrate thermal resistance stays the same, the decrease of the relative contribution of across-the-plane thermal conductance for smaller thicknesses may play a role in the observed reduction of thermal conductance. The dependence on L (Figure 2d) is weaker than that on A (Figure 2c) and in all cases the value of V_{out} - V_{SiO2} for InSe is larger than for bare SiO_2.

Previous studies of different 2D materials have demonstrated a size-dependent phonon transport.[45, 48-51] The value of κ decreases with decreasing the size of the sample as a result of an increase in phonon-boundary scattering. For free-standing graphene, κ decreases from 1700 W m^{-1} K^{-1} to 250 W m^{-1} K^{-1} when the graphene domain size is reduced from 9 μm to 300 nm.[48] A similar dependence was observed in graphene on SiO_2, where κ decreases from 580 W m^{-1} K^{-1} to 280 W m^{-1} K^{-1} going from 10 μm to 260 nm.[50] For single layer InSe, the calculated value of κ decreases from 27.60 W m^{-1} K^{-1} to 8.2 W m^{-1} K^{-1} when reducing the sample size from 10 μm to 100 nm at T = 300 K (**Figure 3**).[24] A similar behavior was predicted by Pandey *et al.*, although the values of κ are larger by ~ 40%.[25] In both models, κ gives the summed contribution of thermal conductivity from all phonon modes, as derived from first-principle Peierls-Boltzmann transport theory for single layer InSe. As shown in Figure 3, the measured normalized dependence of $[V_{out} - V_{SiO2}]^{-1}$ ($\propto\kappa$) on the flake size ($A^{1/2}$) is in qualitative agreement with these models.

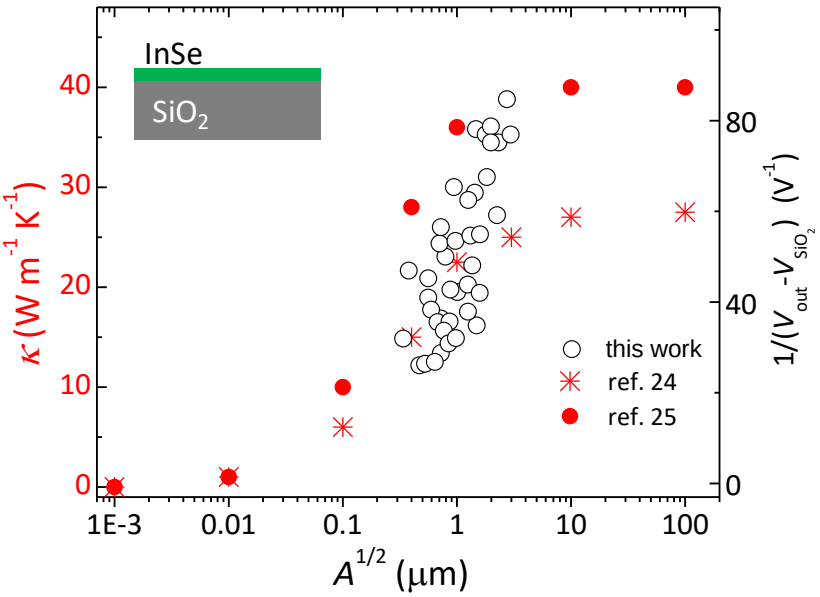

Figure 3. Thermal properties of 2D InSe: dependence on lateral size. Measured dependence of $[V_{out}\text{-}V_{SiO2}]^{-1}$ on $A^{1/2}$ for InSe flakes on a SiO_2/Si substrate (circles), where A is the measured in-plane area of the flake. The measured dependence is compared with the calculated dependence of the thermal conductivity κ on the lateral size of single layer InSe (red symbols).[24-25]

Both the experimentally measured and predicted values of in-plane κ for InSe are significantly smaller than for graphene and other 2D materials, such as hBN or black phosphorus, or than in silicon ($\kappa_{Si} = 145$ W m^{-1} K^{-1}) or copper ($\kappa_{Cu} = 400$ W m^{-1} K^{-1}).[52-53] To explain this difference, we consider the atomic vibrations that carry most of the heat in InSe. In-plane acoustic phonons (transverse (TA) and longitudinal (LA)) and out-of-plane flexural phonon modes (ZA) carry most of the heat in the plane of the flake.[24-25] These are dominated by the vibrations of the heavy indium atoms and have higher group velocity than those of optical phonons. The group velocity for the ZA modes is smaller than for the TA and LA phonons, which have velocities of 1853 m s^{-1} and 3272 m s^{-1}, respectively.[25] Furthermore, optical phonons have a relatively low frequency, providing strong scattering channels for acoustic modes and hence leading to short phonon transport lifetimes and a low κ. Reducing

the length scale for phonon transport reduces further the values of κ, as observed in our experiments and previous theory studies for $A^{1/2} < 1$ μm (Figure 3).

The dependence of the SThM response on L (Figure 2d) indicates that the thermal conductance halves in few-layer InSe flakes (L = 1-5). We assign this behavior to phonon-boundary surface scattering and to the modified phonon dispersions due to quantum confinement. The phonon coherence length tends to decrease proportionally with decreasing L and phonon modes change only in a few layers InSe (Supplementary Information S1).[54] Atomic displacement studies show that whereas optical modes are mostly confined within the InSe layers, acoustic modes that dominate the heat transport are spatially delocalized along the vdW layers. Thus, the latter are more strongly affected in atomically thin layers.

The ability of InSe flakes to conduct heat can be affected by phonon scattering due to impurities.[55] Although our InSe crystals are nominally undoped, they were grown from an indium-rich melt of components with a non-stoichiometric composition of $In_{1.03}Se_{0.97}$[56] that facilitates the formation of indium-interstitial atoms and n-type conductivity ($n \sim 10^{16}$ cm^{-3}).[57] The interface of 2D InSe with the supporting SiO_2 substrate can also play an important role. The two interfaces interact elastically via vdW and Coulomb forces. Due to the strong dependence of the potential energy on distance, the increase in the separation between the layer and its supporting substrate caused by an imperfect interface/ionized defects and large electron-phonon interaction in InSe can change the ability of phonons to be transmitted across the interface.[27, 58] Studies of coherent phonon transport by picosecond ultrasonics have revealed large (~10 μm^2) regions of "broken" interfaces where the InSe layers are weakly coupled to the supporting SiO_2 substrate due to surface roughness of SiO_2 and contamination at the InSe/SiO_2 interface.[58-59] Thus, thermal coupling between InSe and SiO_2 is reduced, causing an interfacial thermal resistance and suppressed heat dissipation from the flake. The InSe flake under the SThM probe can be overheated and appears hotter (*i.e.* less thermally

conductive) than the surrounding SiO_2 (Figure 1c). To assess further the role of the substrate, we have examined free-standing flakes as well as flakes supported by different substrates.

2.3. Free-standing InSe

Figures 4a and b show AFM and SThM images of a representative 12 nm-thick (*i.e.* $L = 14$) InSe flake over an array of 3 μm-wide microwells. The inset in Figure 4b shows a zoomed-in SThM image of the free-standing flake on an individual microwell (see also schematic in Figure 4c).

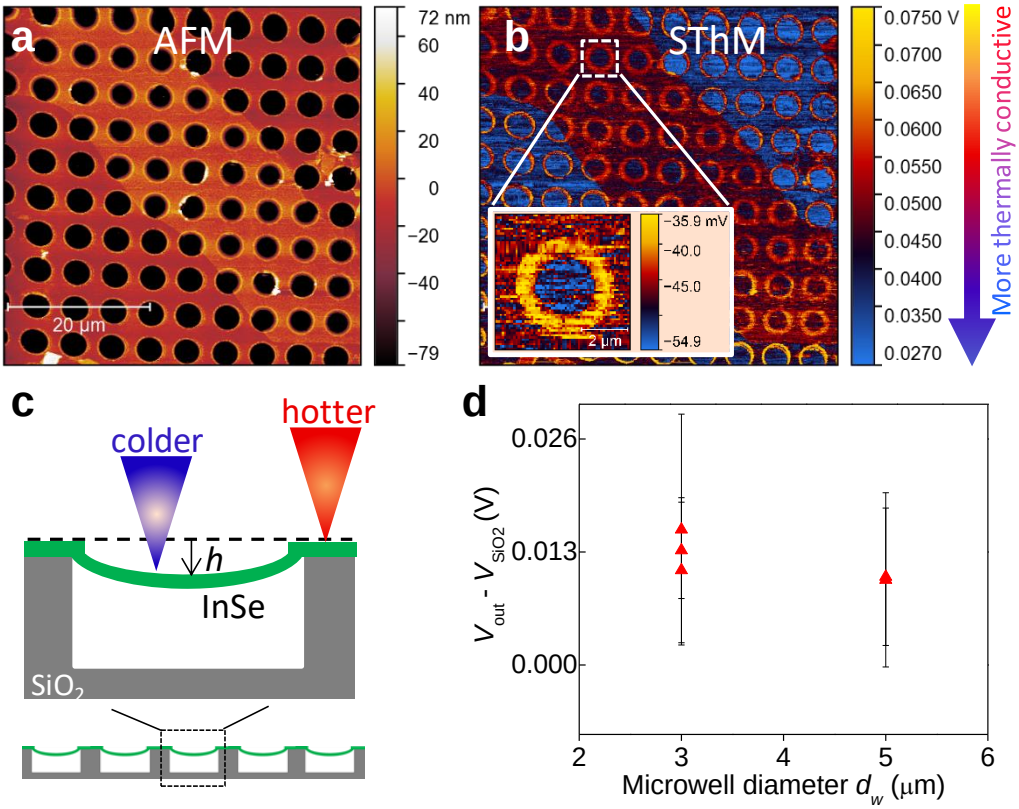

Figure 4. Thermal properties of free-standing InSe. AFM **(a)** and SThM **(b)** images of a 12 nm-thick ($L = 14$) InSe flake that is free-standing over an array of 3 μm-wide cylindrical microwells on a SiO_2 substrate. The inset in part **(b)** shows a zoomed-in region of the SThM For the preparation of free-standing InSe, freshly exfoliated flakes were dry-transferred onto periodic arrays of cylindrical microwells, which were pre-etched onto SiO_2 (see Experimental Section). The microwells are equally spaced by a distance $l_w = 1.5$ μm and have depth, $h_w = 95$ nm, and diameter, $d_w = 3$ μm or 5 μm.

In Figure 4b the free-standing part of the flake appears in dark blue (*i.e.* higher κ), whereas the surrounding regions, corresponding to the substrate supported flake, are red (*i.e.* lower κ). Thus, the SThM image indicates that the free-standing InSe is more thermally conducting than InSe on SiO_2. This effect is observed in all our free-standing InSe flakes (L from 12 to 26 layers, not shown). We assign the reduced thermal transport in InSe/SiO_2 to phonon scattering by interface defects due to surface roughness of SiO_2 and/or contaminants trapped at the InSe/SiO_2 interface. As for other 2D materials (including single- and few-layer graphene,[47, 60-62] single- and bilayer MoS_2 and $MoSe_2$,[63] *etc.*), a substrate can lower the value of κ (*e.g.* by up to a factor of 2.5 for MoS_2 and $MoSe_2$, and 5 for graphene).

As shown in the SThM image of Figure 4b-inset, the edge of the microwell appears as a bright yellow ring, indicating a lower thermal conductance compared to the substrate supported or free-standing regions of InSe. While this could be a topographical artefact due to decreased contact area between the tip and the surface, it can also arises from the localized decrease of κ due to a strain effect: at the edges of the microwells, the InSe flake is bent and thus subjected to tensile strain (Figure 4c). The latter assignment is confirmed by micro-Raman spectroscopy images (Supplementary Information S2) revealing a Raman red shift of the vibrational modes $A_1'(\Gamma_1^2)$ and $A_1'(\Gamma_1^3)$ at the microwell edges. Tensile strain in bent InSe can shift these Raman modes [14, 64] and enhance anharmonic phonon scattering, reducing phonon group velocity and heat capacity.[31] Specifically, a reduction of κ from 25.9 W m^{-1} K^{-1} to 13.1 W m^{-1} K^{-1} was predicted under a strain of 6%.[31] First-principles calculations indicate that the lattice thermal conductivity of micron-sized (2 μm - 200 μm) InSe monolayers decreases linearly as the applied tensile strain increases from 0.5% to 13%.[33]

The suspended depth (h) of the free-standing InSe flake regions into the microwell varies from one microwell to another from h = 74 nm to 82 nm. However, in all cases the value of V_{out} - V_{SiO2} for the free-standing regions is lower (*i.e.* higher κ) than that of the InSe

regions on SiO_2, but closer to that of SiO_2 as h and hence strain increase (Supplementary Information S3).

Finally, we examine free-standing InSe flakes on microwells with different diameter d_w. Flakes suspended over 5 μm-wide microwells tend to show a slightly higher thermal conductance (*i.e.* lower V_{out} -V_{SiO2}) than those over 3 μm-wide ones (Figure 4d). To eliminate the effect of the flake size, only large flakes were considered for this comparison (L > 10 and A > 7 μm^2), *i.e.* flakes with dimensions at which κ does not depend on L and/or A. This behavior resembles that reported in other suspended 2D materials: for MoS_2, WS_2 and WSe_2[51, 65-67] κ increases with increasing size, d, of the suspended flake due to the anharmonicity of the phonon potential and boundary scattering.[67] Although the phonon mean free path of these 2D materials is only a few tens of nanometers, which is orders of magnitude smaller than the suspended lengths of the flakes, κ increases by a factor of about 3 going from d = 2 μm to 13 μm.[67] The thermal transport is defined by a broad spectrum of phonons with various polarizations and frequencies. In particular, phonons with long mean free path of up to 20 μm at T = 300 K in InSe can make a significant contribution to κ.[24]

2.4. InSe on different substrates

The choice of the substrate and/or capping material offers means to modulate the thermal response of a 2D material, but requires an understanding of interface interactions and heat exchange mechanisms between materials. Previous Raman studies of InSe flakes have shown that the thermal conductivity can be significantly enhanced by a substrate or a capping layer with high κ, such as Al_2O_3 (κ_{Al2O3} = 50 W m^{-1} K^{-1}), which can facilitate heat dissipation and charge-phonon interactions at the InSe/Al_2O_3 interface.[26-27] The estimated value of κ for a 4 nm-thick (L = 5) InSe flake on Al_2O_3 was found to be κ = 53.4 W m^{-1} K^{-1}, higher than on

SiO_2 ($\kappa = 28.7$ W m^{-1} K^{-1}).[27] Here, we use SThM to probe the substrate-induced modification of the thermal response of InSe. For this study, we transferred InSe flakes on substrates with κ that is either lower or higher than that of SiO_2 (κ_{SiO2} = 1.4 W m^{-1} K^{-1})[37], namely PMMA (κ_{PMMA} = 0.21 W m^{-1} K^{-1})[68] and multilayer hBN (κ_{hBN} = 400 W m^{-1} K^{-1})[69-70], respectively.

InSe flakes were exfoliated and transferred onto a periodic array of PMMA-micropillars on a SiO_2/Si substrate (see Experimental Section). The micropillars are equally spaced by a distance l_p = 1 μm and have width, w_p = 1 μm, and average height, $h_p \approx$ 16 nm. **Figures 5**a and b show AFM and SThM images, respectively, of a representative 45 nm-thick (*i.e.* L = 54) InSe flake bent onto the array of PMMA-micropillars. Figure 5c illustrates a schematic representation of a flake bent over the array. In the SThM image of Figure 5b, the substrate-supported part of the InSe flake is red-colored, whereas the bare PMMA-micropillars appear as bright yellow (*i.e.* lower κ) circular spots on the dark blue (*i.e.* higher κ) background of the SiO_2 substrate. This indicates that InSe has a lower κ than SiO_2, but higher than that of the bare PMMA-micropillars. The inset in Figure 5b shows a zoomed-in SThM image of an individual micropillar with an InSe flake bent over it, revealing a yellow circular region (*i.e.* lower κ) at the location of the pillar, whereas the surrounding area, corresponding to the layer supported by the SiO_2 substrate, is dark blue-colored (*i.e.* higher κ). Hence, InSe on PMMA-micropillars is less thermally conductive than on SiO_2. This can also be seen in Figure 5d, which plots together AFM height and SThM response profiles for several InSe-capped PMMA-micropillars, as measured simultaneously along the line marked in Figures 5a and b, respectively. There is a good correlation between the two data sets with peaks in V_{out} - V_{SiO2} (*i.e.* drops in κ) matching the positions of the pillars. A similar response was obtained for flakes with different number of layers.

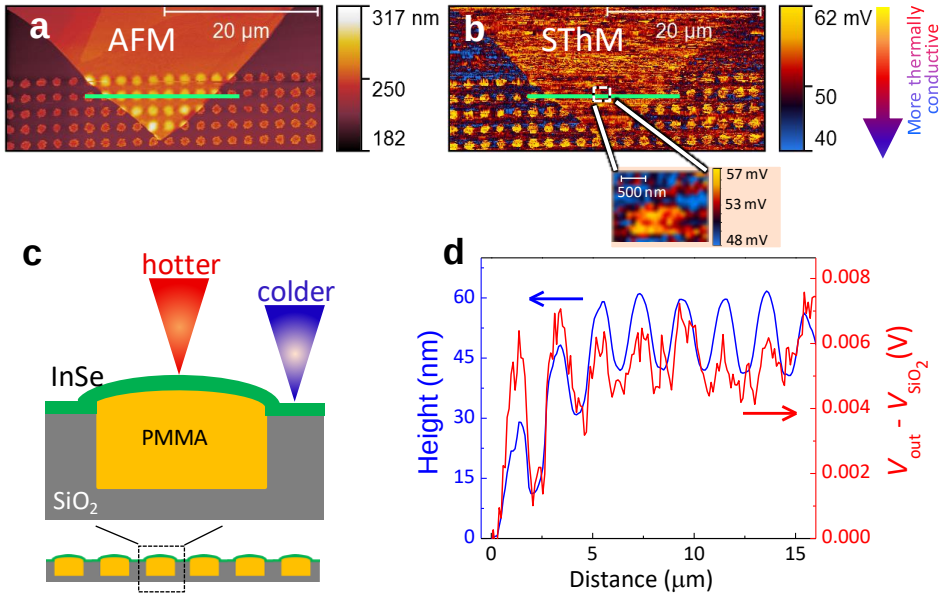

Figure 5. Thermal properties of InSe supported by PMMA-micropillars. AFM **(a)** and SThM **(b)** images of a 45-nm thick (L = 54) InSe flake transferred onto an array of PMMA-micropillars with average height of ~16 nm and width of 1 µm. The green lines mark the AFM and SThM profiles shown in part **(d)**. The inset in part **(b)** shows a zoomed-in SThM image of a region of the InSe flake supported by an individual micropillar, enclosed in the dotted square. **(c)** Schematic representation of the heat conduction for a flake supported by the micropillars. **(d)** AFM and SThM profiles along the green lines shown in parts **(a)** and **(b)**.

We assign the low thermal conductance of InSe on PMMA compared to InSe on SiO_2 (Figures 5b and d) to the low value of κ for PMMA (κ_{PMMA} = 0.21 W m^{-1} K^{-1}),[68] which reduces the ability of InSe to dissipate heat. Similar effects were also observed in graphene, where the κ values of PMMA supported layers were found to be reduced down to 360 W m^{-1} K^{-1}, which is about half of the value for graphene on SiO_2 and an order of magnitude lower than for free-standing graphene.[68] This lower thermal conductance is a limiting factor in the thermal management of recent InSe-based FETs, where PMMA provides electrical stability and increases the electrical conductivity compared to InSe/SiO_2 FETs.[71-72] We also note that PMMA is widely used in the fabrication of 2D materials, for example as a carrier layer in deterministic transfer of flakes to assemble vdW heterostructures and as a standard electron-beam lithography resist.[73] Almost unavoidably, this results in PMMA residues

remaining on the surfaces of 2D layers or at their interfaces, even after cleaning.[74] In addition, PMMA is used to encapsulate 2D structures, including InSe FETs, to enhance their stability under ambient conditions.[71-72] Thus, the presence of PMMA, even in a form of local inclusions in 2D materials, can substantially distort the thermal transport leading to overheating. On the other hand, the use of a low-κ flexible dielectrics compatible with InSe, such as PMMA, can be beneficial for thermoelectrics.[71]

A substrate-induced enhancement of κ would naturally be expected from a material with high κ, such as hBN, which has the second largest κ per unit weight among all insulating and semiconducting compounds.[70] Furthermore, since hBN is electrically insulating, it could provide an excellent heat spreader in 2D technologies.[75] However, our SThM of InSe on hBN did not reveal any significant increase in thermal conductance compared to InSe on SiO_2 (Supplementary Information S4). This unexpected result could potentially originate from strain caused by lattice mismatch ($\varepsilon = [a_{InSe} - a_{hBN}]/a_{InSe} \approx 37\%$),[76-77] thermal expansion mismatch and/or rotational crystal misalignment. These factors can affect the thermal resistance at the interface of 2D vdW crystals.[78-80] In our samples, the InSe and hBN flakes were randomly stacked without an intentional lattice alignment. Also, we cannot exclude the possibility of contaminants being trapped between the vdW flakes during the polymer-assisted fabrication, which would cause significant perturbation of interface coupling, thus reducing thermal conductance. Although all the exfoliated flakes of InSe and hBN were thoroughly selected and inspected with dark-field optical microscopy at each stage of processing to avoid any visible contaminants or defects (see Experimental Section) and the AFM images of the resulting heterostructures reveal flat and clean layers (Supplementary Information S4), the polymer residues can still be present at the interface in the form of atomically thin films that are difficult to detect by optical microscopy or AFM.[74] Further advances in the current technology of assembly of vdW heterostructures, relying on polymer-

free exfoliation and transfer methods, are required to address this issue. Atomically thin layers to improve thermal coupling with a supporting substrate should also be explored.[81]

3. Conclusion

In summary, 2D InSe has opened promising directions in science and technology, but its thermal response should be carefully considered and tailored for specific studies and applications. The imaging capability of scanning thermal microscopy and its high spatial resolution have enabled us to investigate how the surface topography of a 2D InSe flake and its supporting substrate influence the thermal response. Our investigation of 2D InSe flakes with different size and/or non-uniform topography and systems where the layers are supported by different substrates have revealed a low thermal conductance for 2D InSe, lower than in low-κ SiO_2. This anomalous finding contrasts with previous theoretical studies in the literature, where the role of the substrate was not taken into account. The ability of 2D InSe to conduct heat depends on the thermal interfacial resistance between InSe and the supporting substrate, number of layers, lateral size, and/or strain. It decreases with a decreasing number of layers ($L \leq 5$) and/or flake area ($A < 2$ μm^2). This behavior is consistent with earlier theoretical studies of 2D InSe and is attributed to phonon-boundary surface scattering and to the modified phonon dispersions due to quantum confinement. Enhanced phonon scattering by impurities and/or strain can further influence the thermal conductivity, as discussed for layers transferred onto microwells and micropillars. These experimental findings are important for advancing the use of InSe in thermoelectric technologies that can benefit from the exceptional combination of the unusually low-κ and high electron mobility of this 2D material. We also note that improving the ability of 2D InSe to dissipate heat in nanoelectronics should be further examined by the implementation of high-κ dielectrics, such

as hBN. Advances in the controlled fabrication of multilayered InSe/hBN stacks will be required to address this important future development.

4. Experimental Section

Crystal growth and exfoliation of flakes: The InSe crystals were grown using the Bridgman method from a polycrystalline melt of $In_{1.03}Se_{0.97}$. The crystal structure and γ-phase were assessed by X-ray diffraction studies: the rhombohedral unit cell has lattice parameters $a = b = 4.002$ Å and $c = 24.961$ Å. InSe flakes of various thicknesses were prepared from the as-grown crystals by mechanical exfoliation using adhesive tape and then transferred onto a SiO_2/Si (290 nm-thick SiO_2) substrate. Prior to exfoliation, the substrate was ultrasonically cleaned in acetone and 2-propanol. The bath was applied for 10 minutes for each solvent. The substrate was subsequently cleaned with deionized water and then subjected to oxygen plasma to ensure the removal of any ambient adsorbent or organic molecule on the surface. The InSe flakes were exfoliated using a Nitto ELP-BT-150P-LC tape, with the first layers of exfoliated material being sacrificed to avoid air-exposed material. The InSe on the tape was then brought into contact with the surface of the substrate. The back side of the tape was rubbed with a small rolling pin for 5 minutes to increase the yield of flakes attached to the SiO_2 surface. Finally, the tape was peeled off from the substrate. Optical inspection revealed the successful transfer of several few-layer InSe flakes on the substrate.

Fabrication of free-standing and PMMA supported InSe layers: Free-standing and PMMA supported InSe flakes were fabricated by a combination of standard electron beam lithography (EBL) and mechanical exfoliation of a bulk Bridgman grown γ-InSe crystal. Firstly, an array of circles with diameters of 1 μm, 3 μm and 5 μm were defined by EBL on an oxidized Si wafer with a SiO_2 thickness of 290 nm. Then reactive ion etching was used to etch the circles into cylindrical wells with a nominal depth of 95 nm. Thin layers of γ-InSe were mechanically

exfoliated on a PMMA membrane using the Nitto Denko ELP-BT-150P-ALC tape. The PMMA membranes were then peeled on to the 3 μm and 5 μm cylindrical wells leaving the InSe layers covering the wells. To remove the polymer on the surface of InSe, the sample was cleaned by its full immersion in a bath of acetone and then 2-proponal, for 5 minutes in each. For a second set of samples, the PMMA/InSe membranes were deposited on 1 μm cylindrical wells and immersed in acetone and then 2-propanole, for 5 minutes in each. The microwells were then filled with PMMA, forming micropillars on the SiO_2/Si substrate.

Fabrication of InSe/hBN heterostructures: Firstly, hBN layers were exfoliated using the Nitto Denko ELP-BT-150P-ALC tape on an oxidized Si wafer with a SiO_2 thickness of 290 nm. Suitable flakes were then identified using an optical microscope. Secondly, few-layer γ-InSe flakes were exfoliated using the Nitto Denko ELP-BT-150P-ALC tape onto a PMMA membrane and peeled-off onto the selected hBN flakes using a bespoke micromanipulation setup. To remove the polymer on the surface of the InSe/hBN heterostructure, the sample was cleaned by full immersion in acetone, and then 2-proponal, for 5 minutes in each.

Scanning Thermal Microscopy: SThM operates by biasing a voltage across a Wheatstone bridge, which comprises two known resistors, a variable resistor and the probe resistance of the SThM tip (Figure 1a). The SThM tip is used as a local heater and the fractional change in its resistance is used to detect the temperature and/or the thermal conductance of the sample. Before the measurements (when the tip is millimeters above the sample surface), the variable resistor is adjusted to null the voltage across the bridge. For the measurements presented here, the tip is heated to an equilibrium temperature by controlling the current flowing through it. The sample is a passive component and is heated only by the probe tip once in contact as the heat flows from the tip into the sample. In turn, the tip's temperature decreases, leading to a reduced resistance that unbalances the bridge, as measured by V_{out}. The magnitude of the measured voltage is thus related to the thermal conductance of the sample in contact with the

tip. By monitoring V_{out}, one can create a thermal conductance map of the sample. A standard commercial setup operating in air was used in this study. In the analysis of the data, the heat loss from the cantilever, air conduction/convection that affects the cantilever-sample distance, and, hence, flake thickness, the tip-sample interfacial thermal resistance (which might differ significantly for the probe in contact with InSe, SiO_2, PMMA and hBN) and heat propagation radius have not been taken into account. These simplifying assumptions prevent us from determining directly the thermal conductivity from the measured thermal conductance.[82-83] The SThM tip used for our experiments is a KNT-SThM-2an Resistive Tip (resistance $R \approx$ 325 Ω at 25 °C; sensitivity of ≈1 Ω $°C^{-1}$). Typically, scans containing 512 × 512 pixels were performed at a line rate of 0.1 Hz. The Wheatstone bridge was biased with 1 V, with a 1000× gain used on the amplifier (the maximum sensitivity of the Anasys NanoIR2s microscope). Feedback gains were varied to ensure trace and retrace matched for both the topography and the SThM signal. The Wheatstone bridge was zeroed in air with the tip 2 mm away from the surface and held for 30 minutes to ensure that no drift of the bridge and that the tip reached an equilibrium temperature, before the tip was contacted onto the sample and scanned. All data analyzed were taken from the retrace direction.

X-ray diffraction studies: these studies were conducted using a DRON-3 X-ray diffractometer with a monochromatic Cu-Kα radiation of wavelength λ = 1.5418 Å.

Raman spectroscopy studies: Raman spectroscopy studies on InSe flakes of different thickness in the Supplementary Information S1 were performed using a Horiba LabRAM HR Raman Microscope. Raman spectroscopy studies in the Supplementary Information S2 were performed using a Renishaw inVia confocal Raman microscope. For the latter, we used a 532 nm excitation laser focused through a 100× objective, with a numerical aperture of 0.85. The laser power incident on the sample was ~85 μW. A 2400 line mm^{-1} diffraction grating was

used. The measurements were taken in high confocality mode, resulting in an estimated spot size of ~450 nm in FWHM.

Supporting Information
Supporting Information is available from the Wiley Online Library or from the authors.

Acknowledgements
D.B. and Z.R.K. contributed equally to this work. This project has received funding from the European Union's Horizon 2020 research and innovation programme under grant agreement Graphene Core3. This work was also supported by the Engineering and Physical Sciences Research Council [grant number EP/M012700/1]; the Nanoscale and Microscale Research Centre (nmRC) at the University of Nottingham; the Royal Society; the Leverhulme Trust; and the National Academy of Sciences of Ukraine. N.B acknowledges Prof. Kostya. S. Novoselov and the European Research Council Synergy Grant Hetero2D. We are grateful to Craig Barton for useful discussions.

Author contributions
Z.R.K., A.P., O.K. (National Physical Laboratory) and A.T. designed the experiments; Z.R.K. and Z.D.K. grew the bulk InSe crystals; E.C. prepared the exfoliated layers; N.B. fabricated the free-standing and PMMA supported InSe layers, and the InSe/hBN heterostructures; D.B. conducted the SThM and AFM studies; O.K. (Lancaster University) conducted preliminary SThM studies on bulk crystals; T.V. and D.M. conducted Raman spectroscopy studies; Z.R.K. and A.P. co-wrote the paper; all authors took part in the discussion and analysis of the data.

Competing financial interest statement
The authors declare that they have no competing financial interests.

Materials and correspondence
Correspondence and material request should be addressed to amalia.patane@nottingham.ac.uk and zakhar.kudrynskyi@nottingham.ac.uk.

Received: ((will be filled in by the editorial staff))
Revised: ((will be filled in by the editorial staff))
Published online: ((will be filled in by the editorial staff))

References

[1] A. K. Geim, I. V. Grigorieva, *Nature* **2013**, *499*, 419.
[2] K. S. Novoselov, A. Mishchenko, A. Carvalho, A. H. Castro Neto, *Science* **2016**, *353*, aac9439.
[3] P. Ajayan, P. Kim, K. Banerjee, *Phys. Today* **2016**, *69*, 38.
[4] N. Mounet, M. Gibertini, P. Schwaller, D. Campi, A. Merkys, A. Marrazzo, T. Sohier, I. E. Castelli, A. Cepellotti, G. Pizzi, N. Marzari, *Nat. Nanotechnol.* **2018**, *13*, 246.
[5] G. W. Mudd, S. A. Svatek, T. Ren, A. Patane, O. Makarovsky, L. Eaves, P. H. Beton, Z. D. Kovalyuk, G. V. Lashkarev, Z. R. Kudrynskyi, A. I. Dmitriev, *Adv. Mater.* **2013**, *25*, 5714.
[6] J. F. Sánchez-Royo, G. Muñoz-Matutano, M. Brotons-Gisbert, J. P. Martínez-Pastor, A. Segura, A. Cantarero, R. Mata, J. Canet-Ferrer, G. Tobias, E. Canadell, J. Marqués-Hueso, B. D. Gerardot, *Nano Res.* **2014**, *7*, 1556.
[7] S. R. Tamalampudi, Y. Y. Lu, U. R. Kumar, R. Sankar, C. D. Liao, B. K. Moorthy, C. H. Cheng, F. C. Chou, Y. T. Chen, *Nano Lett.* **2014**, *14*, 2800.
[8] G. W. Mudd, S. A. Svatek, L. Hague, O. Makarovsky, Z. R. Kudrynskyi, C. J. Mellor, P. H. Beton, L. Eaves, K. S. Novoselov, Z. D. Kovalyuk, E. E. Vdovin, A. J. Marsden, N. R. Wilson, A. Patanè, *Adv. Mater.* **2015**, *27*, 3760.
[9] S. Lei, F. Wen, B. Li, Q. Wang, Y. Huang, Y. Gong, Y. He, P. Dong, J. Bellah, A. George, L. Ge, J. Lou, N. J. Halas, R. Vajtai, P. M. Ajayan, *Nano Lett.* **2015**, *15*, 259.
[10] W. Feng, W. Zheng, W. Cao, P. Hu, *Adv. Mater.* **2014**, *26*, 6587.
[11] D. A. Bandurin, A. V. Tyurnina, G. L. Yu, A. Mishchenko, V. Zolyomi, S. V. Morozov, R. K. Kumar, R. V. Gorbachev, Z. R. Kudrynskyi, S. Pezzini, Z. D. Kovalyuk, U. Zeitler, K. S. Novoselov, A. Patane, L. Eaves, I. V. Grigorieva, V. I. Fal'ko, A. K. Geim, Y. Cao, *Nat. Nanotechnol.* **2017**, *12*, 223.
[12] Y. Li, C. Yu, Y. Gan, Y. Kong, P. Jiang, D. F. Zou, P. Li, X. F. Yu, R. Wu, H. Zhao, C. F. Gao, J. Li, *Nanotechnology* **2019**, *30*, 335703.
[13] Q. Zhao, R. Frisenda, T. Wang, A. Castellanos-Gomez, *Nanoscale* **2019**, *11*, 9845.
[14] Y. Li, T. Wang, M. Wu, T. Cao, Y. Chen, R. Sankar, R. K. Ulaganathan, F. Chou, C. Wetzel, C.-Y. Xu, S. G. Louie, S.-F. Shi, *2D Mater.* **2018**, *5*, 021002.
[15] L. Chen, Z. G. Yu, D. Liang, S. Li, W. C. Tan, Y.-W. Zhang, K.-W. Ang, *Nano Energy* **2020**, *76*, 105020.
[16] G. W. Mudd, M. R. Molas, X. Chen, V. Zólyomi, K. Nogajewski, Z. R. Kudrynskyi, Z. D. Kovalyuk, G. Yusa, O. Makarovsky, L. Eaves, M. Potemski, V. I. Fal'ko, A. Patanè, *Sci. Rep.* **2016**, *6*, 39619.
[17] L. Chen, D. Liang, Z. Yu, S. Li, X. Feng, B. Li, Y. Li, Y. Zhang, K. Ang, presented at 2019 IEEE International Electron Devices Meeting (IEDM), 7-11 Dec. 2019, **2019**.
[18] M. Dai, H. Chen, F. Wang, Y. Hu, S. Wei, J. Zhang, Z. Wang, T. Zhai, P. Hu, *ACS Nano* **2019**, *13*, 7291.
[19] X. Liu, J.-C. Ren, T. Shen, S. Li, W. Liu, *J. Phys. Chem. Lett* **2019**, *10*, 7712.
[20] M. Li, F. S. Yang, Y. C. Hsiao, C. Y. Lin, H. M. Wu, S. H. Yang, H. R. Li, C. H. Lien, C. H. Ho, H. J. Liu, W. Li, Y. F. Lin, Y. C. Lai, *Adv. Funct. Mater.* **2019**, *29*, 1809119.
[21] Z. R. Kudrynskyi, J. Kerfoot, D. Mazumder, M. T. Greenaway, E. E. Vdovin, O. Makarovsky, Z. D. Kovalyuk, L. Eaves, P. H. Beton, A. Patanè, *Commun. Phys.* **2020**, *3*, 16.
[22] M. A. Bhuiyan, Z. R. Kudrynskyi, D. Mazumder, J. D. G. Greener, O. Makarovsky, C. J. Mellor, E. E. Vdovin, B. A. Piot, I. I. Lobanova, Z. D. Kovalyuk, M. Nazarova, A.

Mishchenko, K. S. Novoselov, Y. Cao, L. Eaves, G. Yusa, A. Patanè, *Adv. Funct. Mater.* **2019**, *29*, 1805491.
[23] Z. R. Kudrynskyi, M. A. Bhuiyan, O. Makarovsky, J. D. G. Greener, E. E. Vdovin, Z. D. Kovalyuk, Y. Cao, A. Mishchenko, K. S. Novoselov, P. H. Beton, L. Eaves, A. Patanè, *Phys. Rev. Lett.* **2017**, *119*, 157701.
[24] A. S. Nissimagoudar, J. Ma, Y. Chen, W. Li, *J. Phys.: Condens. Matter* **2017**, *29*, 335702.
[25] T. Pandey, D. S. Parker, L. Lindsay, *Nanotechnology* **2017**, *28*, 455706.
[26] K. Li, Y. Hong, Z. Li, X. Liu, *Appl. Phys. Lett.* **2018**, *113*, 021903.
[27] V. D. Botcha, M. Zhang, K. Li, H. Gu, Z. Huang, J. Cai, Y. Lu, W. Yu, X. Liu, *J. Alloys Compd.* **2018**, *735*, 594.
[28] H. Wang, G. Qin, J. Yang, Z. Qin, Y. Yao, Q. Wang, M. Hu, *J. Appl. Phys.* **2019**, *125*, 245104.
[29] L. W. Sprague, C. Huang, J.-P. Song, B. M. Rubenstein, *J. Phys. Chem. C* **2019**, *123*, 25437.
[30] W. Wan, S. Zhao, Y. Ge, Y. Liu, *J. Phys.: Condens. Matter* **2019**, *31*, 435501.
[31] Q. Wang, L. Han, L. Wu, T. Zhang, S. Li, P. Lu, *Nanoscale Res. Lett.* **2019**, *14*, 287.
[32] A. I. Dmitriev, G. V. Lashkarev, A. A. Baida, Z. D. Kovalyuk, A. Szewczyk, K. Piotrowski, M. Gutowska, *J. Appl. Phys.* **2002**, *92*, 5110.
[33] Z. Zeng, S. Li, T. Tadano, Y. Chen, *J. Phys.: Condens. Matter* **2020**, *32*, 475702.
[34] S. Gomès, A. Assy, P.-O. Chapuis, *Phys. Status Solidi A* **2015**, *212*, 477.
[35] L. Ramiandrisoa, A. Allard, B. Hay, S. Gomes, *Meas. Sci. Technol.* **2017**, *28*, 14.
[36] Y. Zhang, W. Zhu, F. Hui, M. Lanza, T. Borca-Tasciuc, M. Muñoz Rojo, *Adv. Funct. Mater.* **2020**, *30*, 1900892.
[37] H.-C. Chien, D.-J. Yao, M.-J. Huang, T.-Y. Chang, *Rev. Sci. Instrum.* **2008**, *79*, 054902.
[38] S. M. Atakishiev, D. S. Abdinov, G. A. Akhundov, *Phys. Status Solidi B* **1968**, *28*, K47.
[39] D. P. Spitzer, *J. Phys. Chem. Solids* **1970**, *31*, 19.
[40] G. D. Guseinov, A. I. Rasulov, E. M. Kerimova, M. Z. Ismailov, *Phys. Status Solidi B* **1967**, *19*, K7.
[41] S. Zhou, X. Tao, Y. Gu, *J. Phys. Chem. C* **2016**, *120*, 4753.
[42] J. Duvigneau, H. Schönherr, G. J. Vancso, *ACS Nano* **2010**, *4*, 6932.
[43] A. L. Moore, L. Shi, *Mater. Today* **2014**, *17*, 163.
[44] S. Vaziri, E. Yalon, M. Muñoz Rojo, S. V. Suryavanshi, H. Zhang, C. J. McClellan, C. S. Bailey, K. K. H. Smithe, A. J. Gabourie, V. Chen, S. Deshmukh, L. Bendersky, A. V. Davydov, E. Pop, *Sci. Adv.* **2019**, *5*, eaax1325.
[45] C. Evangeli, J. Spiece, S. Sangtarash, A. J. Molina-Mendoza, M. Mucientes, T. Mueller, C. Lambert, H. Sadeghi, O. Kolosov, *Adv. Electron. Mater.* **2019**, *5*, 1900331.
[46] M. Sezgin, B. Sankur, *J. Electron. Imaging* **2004**, *13*, 146.
[47] M. E. Pumarol, M. C. Rosamond, P. Tovee, M. C. Petty, D. A. Zeze, V. Falko, O. V. Kolosov, *Nano Lett.* **2012**, *12*, 2906.
[48] X. Xu, L. F. Pereira, Y. Wang, J. Wu, K. Zhang, X. Zhao, S. Bae, C. Tinh Bui, R. Xie, J. T. Thong, B. H. Hong, K. P. Loh, D. Donadio, B. Li, B. Ozyilmaz, *Nat. Commun.* **2014**, *5*, 3689.
[49] G. Barbarino, C. Melis, L. Colombo, *Phys. Rev. B* **2015**, *91*, 4.
[50] M. H. Bae, Z. Y. Li, Z. Aksamija, P. N. Martin, F. Xiong, Z. Y. Ong, I. Knezevic, E. Pop, *Nat. Commun.* **2013**, *4*, 7.
[51] G. Hwang, O. Kwon, *Nanoscale* **2016**, *8*, 5280.

[52] X. Gu, R. Yang, *Annual Review of Heat Transfer* **2016**, *19*, 1.
[53] D. L. Nika, A. A. Balandin, *J. Phys.: Condens. Matter* **2012**, *24*, 233203.
[54] R. Schwarcz, M. A. Kanehisa, M. Jouanne, J. F. Morhange, M. Eddrief, *J. Phys.: Condens. Matter* **2002**, *14*, 967.
[55] K. H. Lee, M.-W. Oh, H.-S. Kim, W. H. Shin, K. Lee, J.-H. Lim, J.-I. Kim, S.-I. Kim, *Inorg. Chem. Front.* **2019**, *6*, 1475.
[56] A. Chevy, A. Kuhn, M. S. Martin, *J. Cryst. Growth* **1977**, *38*, 118.
[57] G. W. Mudd, A. Patanè, Z. R. Kudrynskyi, M. W. Fay, O. Makarovsky, L. Eaves, Z. D. Kovalyuk, V. Zólyomi, V. Falko, *Appl. Phys. Lett.* **2014**, *105*, 221909.
[58] J. D. G. Greener, A. V. Akimov, V. E. Gusev, Z. R. Kudrynskyi, P. H. Beton, Z. D. Kovalyuk, T. Taniguchi, K. Watanabe, A. J. Kent, A. Patanè, *Phys. Rev. B* **2018**, *98*, 075408.
[59] J. D. G. Greener, E. De Lima Savi, A. V. Akimov, S. Raetz, Z. Kudrynskyi, Z. D. Kovalyuk, N. Chigarev, A. Kent, A. Patanè, V. E. Gusev, *ACS Nano* **2019**, *13*, 11530.
[60] J. H. Seol, I. Jo, A. L. Moore, L. Lindsay, Z. H. Aitken, M. T. Pettes, X. Li, Z. Yao, R. Huang, D. Broido, N. Mingo, R. S. Ruoff, L. Shi, *Science* **2010**, *328*, 213.
[61] Z. Wang, R. Xie, C. T. Bui, D. Liu, X. Ni, B. Li, J. T. Thong, *Nano Lett.* **2011**, *11*, 113.
[62] W. Cai, A. L. Moore, Y. Zhu, X. Li, S. Chen, L. Shi, R. S. Ruoff, *Nano Lett.* **2010**, *10*, 1645.
[63] X. Zhang, D. Sun, Y. Li, G. H. Lee, X. Cui, D. Chenet, Y. You, T. F. Heinz, J. C. Hone, *ACS Appl. Mater. Interfaces* **2015**, *7*, 25923.
[64] C. Song, F. Fan, N. Xuan, S. Huang, C. Wang, G. Zhang, F. Wang, Q. Xing, Y. Lei, Z. Sun, H. Wu, H. Yan, *Phys. Rev. B* **2019**, *99*, 195414.
[65] X. Gu, R. Yang, *Appl. Phys. Lett.* **2014**, *105*, 131903.
[66] K. Xu, A. J. Gabourie, A. Hashemi, Z. Fan, N. Wei, A. B. Farimani, H.-P. Komsa, A. V. Krasheninnikov, E. Pop, T. Ala-Nissila, *Phys. Rev. B* **2019**, *99*, 054303.
[67] Y. F. Yu, T. Minhaj, L. J. Huang, Y. L. Yu, L. Y. Cao, *Phys. Rev. Appl.* **2020**, *13*, 034059.
[68] J. Liu, T. Wang, S. Xu, P. Yuan, X. Xu, X. Wang, *Nanoscale* **2016**, *8*, 10298.
[69] I. Jo, M. T. Pettes, J. Kim, K. Watanabe, T. Taniguchi, Z. Yao, L. Shi, *Nano Lett.* **2013**, *13*, 550.
[70] Q. Cai, D. Scullion, W. Gan, A. Falin, S. Zhang, K. Watanabe, T. Taniguchi, Y. Chen, E. J. G. Santos, L. H. Li, *Sci. Adv.* **2019**, *5*, eaav0129.
[71] J. Jiang, J. Li, Y. Li, J. Duan, L. Li, Y. Tian, Z. Zong, H. Zheng, X. Feng, Q. Li, H. Liu, Y. Zhang, T.-L. Ren, L. Han, *npj 2D Mater. Appl.* **2019**, *3*, 29.
[72] G. Liang, Y. Wang, L. Han, Z.-X. Yang, Q. Xin, Z. R. Kudrynskyi, Z. D. Kovalyuk, A. Patanè, A. Song, *Semicond. Sci. Technol.* **2018**, *33*, 06LT01.
[73] R. Frisenda, E. Navarro-Moratalla, P. Gant, D. Pérez De Lara, P. Jarillo-Herrero, R. V. Gorbachev, A. Castellanos-Gomez, *Chem. Soc. Rev.* **2018**, *47*, 53.
[74] I. Gasparutti, S. H. Song, M. Neumann, X. Wei, K. Watanabe, T. Taniguchi, Y. H. Lee, *ACS Appl. Mater. Interfaces* **2020**, *12*, 7701.
[75] Y. Fu, J. Hansson, Y. Liu, S. Chen, A. Zehri, M. K. Samani, N. Wang, Y. Ni, Y. Zhang, Z.-B. Zhang, Q. Wang, M. Li, H. Lu, M. Sledzinska, C. M. S. Torres, S. Volz, A. A. Balandin, X. Xu, J. Liu, *2D Mater.* **2020**, *7*, 012001.
[76] A. Davies, J. D. Albar, A. Summerfield, J. C. Thomas, T. S. Cheng, V. V. Korolkov, E. Stapleton, J. Wrigley, N. L. Goodey, C. J. Mellor, A. N. Khlobystov, K. Watanabe, T. Taniguchi, C. T. Foxon, L. Eaves, S. V. Novikov, P. H. Beton, *Nano Lett.* **2018**, *18*, 498.

[77] N. Balakrishnan, Z. R. Kudrynskyi, M. W. Fay, G. W. Mudd, S. A. Svatek, O. Makarovsky, Z. D. Kovalyuk, L. Eaves, P. H. Beton, A. Patanè, *Adv. Opt. Mater.* **2014**, *2*, 1064.
[78] H. Li, H. Ying, X. Chen, D. L. Nika, A. I. Cocemasov, W. Cai, A. A. Balandin, S. Chen, *Nanoscale* **2014**, *6*, 13402.
[79] Y. Gao, Q. Liu, B. Xu, *ACS Nano* **2016**, *10*, 5431.
[80] C.-C. Chen, Z. Li, L. Shi, S. B. Cronin, *Appl. Phys. Lett.* **2014**, *104*, 081908.
[81] M. M. Sadeghi, I. Jo, L. Shi, *Proc. Natl. Acad. Sci. U.S.A.* **2013**, *110*, 16321.
[82] D. G. Cahill, W. K. Ford, K. E. Goodson, G. D. Mahan, A. Majumdar, H. J. Maris, R. Merlin, S. R. Phillpot, *J. Appl. Phys.* **2003**, *93*, 793.
[83] J. Spiece, C. Evangeli, K. Lulla, A. Robson, B. Robinson, O. Kolosov, *J. Appl. Phys.* **2018**, *124*, 015101.

The ability of atomically-thin InSe to conduct heat is probed by scanning thermal microscopy. This reveals an anomalous low thermal conductivity that decreases with reducing the lateral size and thickness of InSe, under strain and in layers weakly coupled to a substrate. These properties are critical for future emerging technologies.

D. Buckley, Z. R. Kudrynskyi*, N. Balakrishnan, T. Vincent, D. Mazumder, E. Castanon, Z. D. Kovalyuk, O. Kolosov, O. Kazakova, A. Tzalenchuk, and A. Patanè*

Anomalous low thermal conductivity of atomically thin InSe probed by scanning thermal microscopy

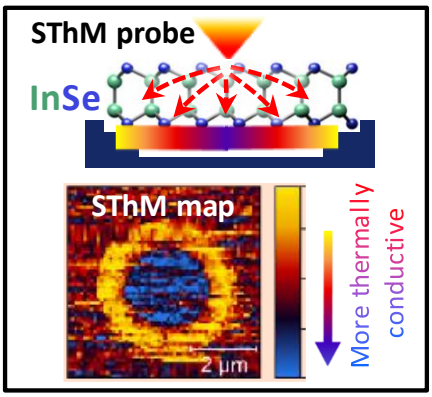

Supporting Information

Anomalous low thermal conductivity of atomically thin InSe probed by scanning thermal microscopy

David Buckley, Zakhar R. Kudrynskyi, Nilanthy Balakrishnan, Tom Vincent, Debarati Mazumder, Eli Castanon, Zakhar D. Kovalyuk, Oleg Kolosov, Olga Kazakova, Alexander Tzalenchuk, and Amalia Patanè**

S1. Raman spectroscopy of InSe with different layer thickness

Distinct Raman peaks can be seen in flakes with thickness ≥ 5 layers (*L*), corresponding to different vibrational modes, as sketched in the Figure. The intensity of the Raman peaks decreases with decreasing *L*. The position of some of the Raman lines is modified in few-layer flakes (~ 5*L*). No clear peaks can be seen below 5 layers.

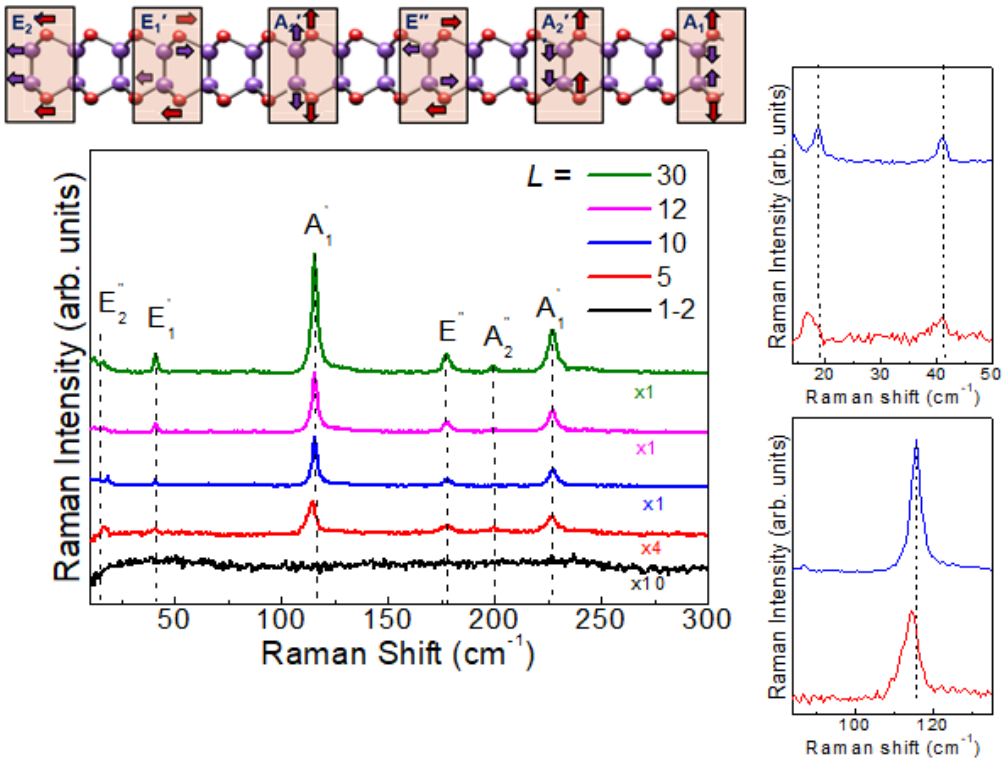

Figure S1. Room temperature (*T* = 300 K) micro-Raman spectra for InSe flakes with different number of layers *L*. The top inset illustrates different Raman modes. The right insets compare specific Raman modes for *L* = 10 (blue) and 5 (red) layers. The spectra were acquired with laser light of wavelength λ= 532 nm and *P* = 0.2 mW. The positions of the Raman modes and their dependence on the layer thickness are similar to those reported in the literature for γ-InSe.[54]

S2. Raman spectroscopy of strained InSe on SiO_2 microwell

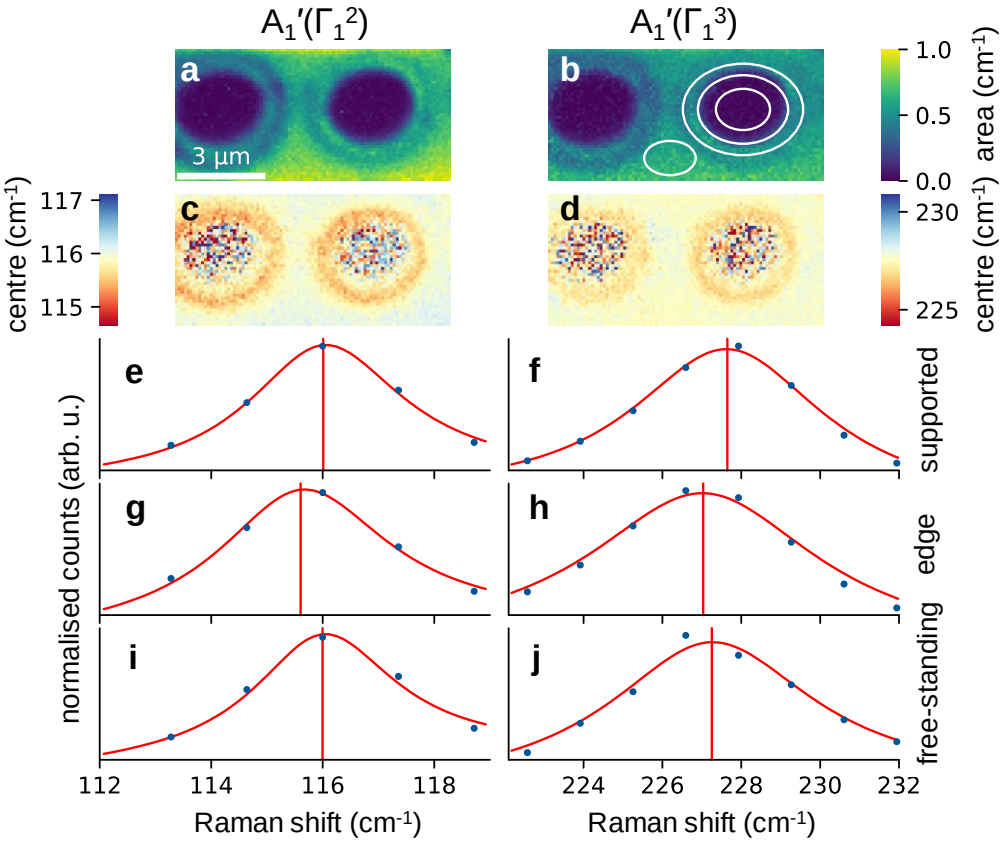

Figure S2. Raman spectroscopy of a 12 nm-thick (L = 14) InSe flake that is free-standing over a 3 μm-wide cylindrical microwell on a SiO_2 substrate. Color maps of the micro-Raman peak area (**a** and **b**) and peak position (**b** and **c**) for $A_1'(\Gamma_1^2)$ and $A_1'(\Gamma_1^3)$ vibrational modes, respectively. Single Raman spectra of substrate supported (**e** and **f**), microwell edge (**g** and **h**) and free-standing (**i** and **j**) regions of the InSe flake for $A_1'(\Gamma_1^2)$ and $A_1'(\Gamma_1^3)$ vibrational modes, respectively. Blue dots denote measured data points and red lines denote fitting curves. All measurements conducted at T = 300 K with λ = 532 nm, P = ~85 μW.

S3. Free-standing InSe on microwells with different suspended depth

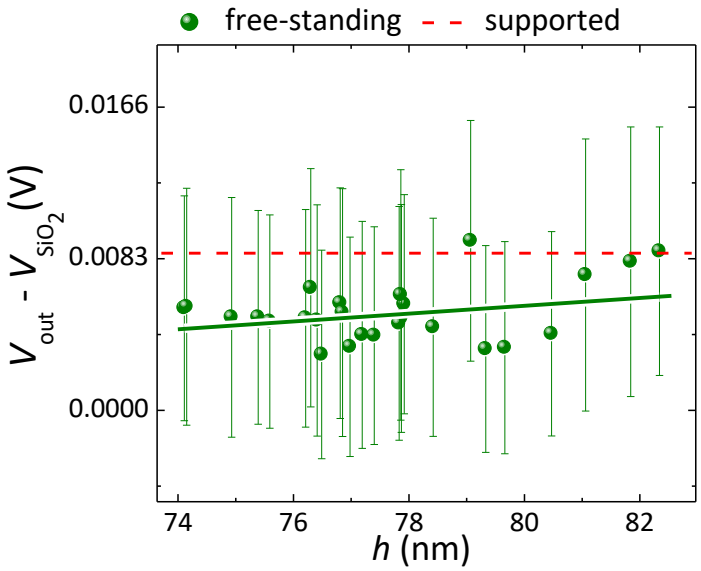

Figure S3. SThM response of a 12 nm-thick (L = 14) InSe flake that is free-standing over 26 different 3 μm-wide cylindrical microwells on a SiO_2 substrate. Here, h is the suspended depth of the flake over each microwell, as sketched in Figure 4c. The solid green line shows a linear fit to the data. The dashed red line is the corresponding average value of the SThM response for the InSe flake on SiO_2.

S4. InSe on hBN

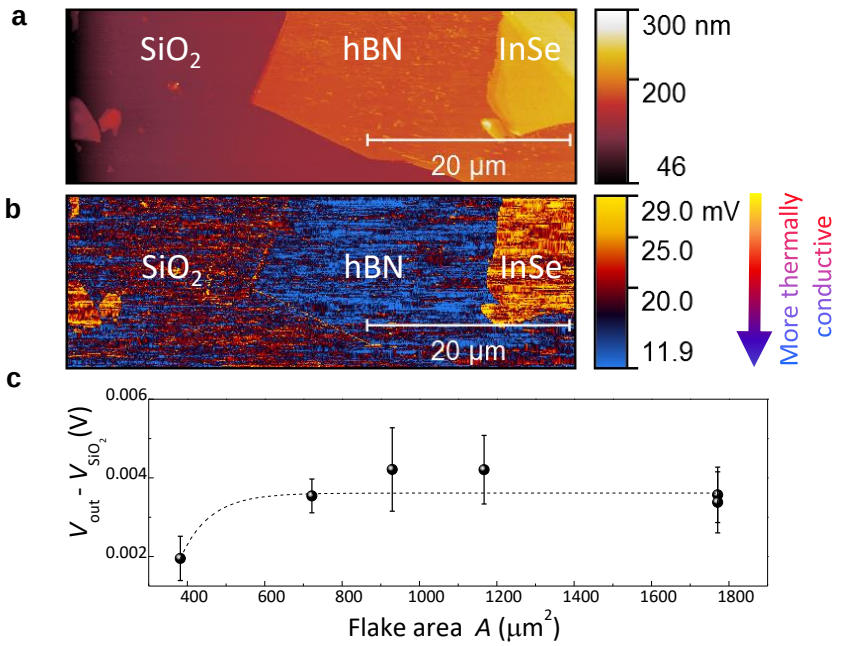

Figure S4. AFM **(a)** and SThM **(b)** images of a 46-nm thick (L = 55 layers) InSe flake stamped on a 51 nm-thick (L = 153 layers) hBN flake exfoliated on a SiO_2 substrate. **(c)** SThM response as a function of the InSe flake area A. The dash line is a guide to the eye. Similar data were obtained for InSe flakes with L ranging from 13 to 82 layers.